

Transcriptomic reveals the ferroptosis features of host response in a mouse model of Zika virus infection

Qian Yan^{1,2,3} | Wenjiang Zheng^{1,2,3} | Yong Jiang⁴ | Peiwen Zhou⁵ |
 Yanni Lai⁶ | Chengxin Liu¹ | Peng Wu¹ | Hongfa Zhuang² |
 Huiting Huang² | Geng Li³ | Shaofeng Zhan^{1,2} | Zizhao Lao^{3,4} |
 Xiaohong Liu^{1,2}

¹Department of Internal Medicine of Traditional Chinese Medicine (TCM), The First Clinical Medical School, Guangzhou University of Chinese Medicine, Guangzhou, China

²Department of Pulmonary and Critical Care Medicine (PCCM), The First Affiliated Hospital, Guangzhou University of Chinese Medicine, Guangzhou, China

³Animal Biosafety Level 2 laboratory (ABSL-2), Animal Laboratory Center, Guangzhou University of Chinese Medicine, Guangzhou, China

⁴Traditional Chinese Medicine Innovation Research Center and Department of Respiratory Medicine, Shenzhen Hospital of Integrated Traditional Chinese and Western Medicine, Shenzhen, China

⁵Animal Biosafety Level 3 laboratory (ABSL-3), Foshan Institute of Medical Microbiology, Foshan, China

⁶Department of Diagnostics of Traditional Chinese Medicine (TCM), Basic Medical Sciences School, Guangzhou University of Chinese Medicine, Guangzhou, China

Correspondence

Shaofeng Zhan and Xiaohong Liu, Department of Pulmonary and Critical Care Medicine (PCCM), The First Affiliated Hospital of Guangzhou University of Chinese Medicine, Guangzhou 510405, China.

Email: zhanshaofeng1680@gzucm.edu.cn and rsclxhgzcum@163.com

Zizhao Lao, Traditional Chinese Medicine Innovation Research Center and Department of Respiratory Medicine, Shenzhen Hospital of Integrated Traditional Chinese and Western Medicine, 518104, Shenzhen, China; Animal Biosafety Level 2 laboratory (ABSL-2), Animal Laboratory Center of Guangzhou University of Chinese Medicine, Guangzhou 510405, China.
 Email: lao_zizhao@163.com

Funding information

The National Natural Science Foundation of China, Grant/Award Number: 82274418; The Key-Area Research and Development Program of Guangdong Province, Grant/Award Number: 2020B111110002; The "Double First-Class" and High-level University Discipline Collaborative Innovation Team Project of Guangzhou University of Chinese Medicine, Grant/Award Number: 2021XK16; The Science, Technology and Innovation Commission of Shenzhen Municipality, Grant/Award Number:

Abstract

Zika virus (ZIKV) is a neurotropic flavivirus. The outbreak of ZIKV in 2016 created a global health emergency. However, the underlying pathogenic mechanisms remain elusive. We investigated the host response features of in vivo replication in a mouse model of ZIKV infection, by performing a series of transcriptomic and bioinformatic analyses of ZIKV and mock-infected brain tissue. Tissue damage, inflammatory cells infiltration and high viral replication were observed in the brain tissue of ZIKV infected mice. RNA-Seq of the brain indicated the activation of ferroptosis pathways. Enrichment analysis of ferroptosis regulators revealed their involvement in pathways such as mineral absorption, fatty acid biosynthesis, fatty acid degradation, PPAR signaling pathway, peroxidase, and adipokinesine signalling pathway. We then identified 12 interacted hub ferroptosis regulators (CYBB, HMOX1, CP, SAT1, TF, SLC39A14, FTL, LPCAT3, FTH1, SLC3A2, TP53, and SLC40A1) that were related to the differential expression of CD8⁺ T cells, microglia and monocytes. CYBB, HMOX1, SALT, and SLAC40A1 were selected as potential biomarkers of ZIKV infection. Finally, we validated our results using RT-qPCR and outside available datasets. For the first time, we proposed a possible mechanism of ferroptosis in brain tissue infected by ZIKV in mice and identified the four key ferroptosis regulators.

JSGG20220226090550002; The Technology Research of COVID-19 Treatment and Prevention and Special Project of Traditional Chinese Medicine Application-Research, Grant/Award Number: 2020KJCX-KTYJ-130; The Sanming Project of Medicine in Shenzhen, Grant/Award Number: SZZYSM202106006

KEY WORDS

differentially expressed genes, ferroptosis, mouse model, transcriptomic, Zika virus

1 | INTRODUCTION

Zika virus (ZIKV) is a pathogen belonging to the Flaviviridae family and is transmitted by mosquitoes. ZIKV was first isolated from a feverish rhesus monkey in 1947¹ and spread in Africa and Asia in 2007. In 2013, Polynesia reported indigenous cases,² and approximately 28 000 people sought medical care due to ZIKV infection, which led to further spread of ZIKV.³ In 2015, Brazil also reported cases of ZIKV.⁴ Subsequently, ZIKV spread to many countries in Oceania, and it was declared a global public health emergency on February 1, 2016.

There is no specific clinical manifestation of ZIKV infection, but it usually manifests as mild fever, rash, joint pain and conjunctivitis.⁵ ZIKV is both neuroinvasive and neurotropic.⁶ It has been reported that ZIKV is associated with fetal microcephaly, spontaneous abortion, and stillbirth during the epidemic in Latin America, and there is evidence that ZIKV can be detected in the amniotic fluid or brain of fetuses with microcephaly.^{7,8} The symptoms associated with ZIKV infection have historically been mild, though more serious complications have been found in the outbreaks of ZIKV infection in the South Pacific and Latin America. During the 2013–2014 ZIKV outbreak in French Polynesia, ZIKV infection showed effects on the nervous system and showed its first association with Guillain-Barré syndrome (GBS).² GBS manifests as an autoimmune peripheral neuropathy that can cause pain, weakness, paralysis, and even nerve paralysis.² Encephalopathy, meningitis, myelitis, and seizures have also been reported in the spectrum of neurological disorders of ZIKV infection in adults.^{6,9,10} Although ZIKV infection is less prevalent now, indigenous mosquito-borne transmission of ZIKV had been recorded in four of the six WHO regions, including Africa, the Americas, Southeast Asia and the Western Pacific by July 2019.¹¹

Particularly, the underlying pathogenic mechanisms of ZIKV infection remain unknown and there is no vaccine or specific antiviral therapy for the disease. Viral infections often lead to cell death. Cell death can inhibit virus replication, but it can also enhance virus transmission and cause tissue damage, aggravating viral infection.¹² Ferroptosis is a regulated, iron-dependent cell death driven by lipid peroxidation. The process differs from apoptosis and other forms of cell death.¹³ In the field of virology, we noticed that HIV-1 is affected by ferroprotein degradation, which can facilitate viral genome transcription.¹⁴ HIV patients with neurocognitive impairment often have iron dysmorphism, which may be related to iron death.¹⁵ A large amount of iron is stored within ferritin in the cells. Targeting ferroptosis may be a useful therapeutic strategy for managing the

hyperinflammation caused by coronavirus infection.¹⁶ The level of ferritin in the cerebrospinal fluid (CSF) may reflect the amount of iron in the brain.¹⁷ Studies suggest that serum iron and ferritin levels are associated with cerebral ischemia or disease severity in COVID-19 patients, suggesting that iron death may occur in the brain of COVID-19 patients.¹⁸ Researchers found that the iron salt ferric ammonium citrate inhibited influenza A virus, HIV virus, ZIKV, and EV71.¹⁹ The findings of these studies highlight the need for further research into how other viruses activate and inhibit ferroptosis. It is still unknown whether ferroptosis plays a role in ZIKV-induced neuronal death in the brain.

The establishment of animal models has contributed to improving the understanding of ZIKV. At present, several models simulating ZIKV infection have been developed, including immunocompromised and immunocompetent mouse models. Studies have shown that ZIKV can replicate in high titers in mice and cause central nervous system (CNS) cell damage.^{20,21} ZIKV-infected *IFNAR*^{-/-} mice (C57BL/6 background mice lacking IFN α/β receptors) develop diseases related to high brain virus titers.²²

In the current study, we challenged the *IFNAR*^{-/-} mice with a ZIKV strain and performed RNA-seq on the mouse brain tissue. We further performed transcriptomic and bioinformatics analyses based on the raw data. We quantified the differences in immune cell expression based on RNA-seq results and linked ferroptosis and immune infiltration for the first time. These may provide direction for the exploration of potential therapeutic targets for ZIKV-infection and the elucidation of molecular mechanisms.

2 | MATERIALS AND METHODS

2.1 | Ethics statements and facility

For virus infection experiments, all animal procedures were approved by the Animal Ethics Committee of Guangzhou University of Chinese Medicine. Studies with ZIKV were carried out under animal biosafety level 2 (ABSL-2) laboratory at the Animal Experiment Center of Guangzhou University of Chinese Medicine.

2.2 | Cell lines and cell culture conditions

We purchased *Aedes albopictus* gut cell lines (C6/36) from the American Type Culture Collection (#CRL-1660). C6/36 cells were

cultured at 30°C in a 5% CO₂ incubator in a minimum essential medium (Gibco) supplemented with 10% fetal bovine serum (Gibco), 100 units/ml of penicillin and 100 µg/ml of streptomycin solution (Pen/Strep; Merck KGaA).

2.3 | Virus amplification

To generate large quantities of ZIKV for use in experiments, C6/36 cells were incubated with ZIKV at a multiplicity of infection of 0.5 for 2 h and then the unbound ZIKV virus was washed away. ZIKV-infected cells were sequentially cultured in a fresh medium containing 2% FBS for 7–10 days. The supernatant was harvested and centrifuged at 4000g for 10 min to remove cellular debris and then filtered through a 0.22 µm filter. Asian ZIKV (GenBank: ZIKV KU963796) was a gift from Guangdong Provincial Center for Disease Control and Prevention.

2.4 | Animal experiments

The male C57BL/6 *IFNAR*^{-/-} mice (*n* = 6) were provided as gifts by Professor Zhao Jincun of the State Key Laboratory of Respiratory Diseases of Guangzhou Medical University, China. The breeding environment was a temperature of 21°C and humidity of 55%. All animals were generated and bred in our laboratory at under specific pathogen-free conditions, allowed to freely eat and drink, and maintained on a 12-h light/dark cycle. Mice were numbered and weighed after 7 days of acclimation and then randomly divided into two groups (*n* = 3 per group): the model group and the control group. Next, *IFNAR*^{-/-} male mice were challenged intraperitoneally with the 1 × 10⁶ PFU of the Asian ZIKV strain per mouse. Mice injected with an equal volume of PBS (mock-infected) were used as negative controls (*n* = 3). Mice were observed daily for weight loss and the development of virus-induced disease. Mice were euthanized with pentobarbital (100 mg/kg, i.v.) on Day 9 postinfection, before humane endpoints were reached (weight loss ≥30%, hunched posture, fur folds, conjunctivitis, dyskinesia, paralysis).²³ Coronal intact sections of brain tissue were used for pathological sectioning and immunofluorescence analysis, and the remaining tissue was stored at -80°C for subsequent RT-qPCR quantification of viral RNA load and RNA-seq analysis.

2.5 | Total RNA isolation and RT-qPCR

Total genomic RNA from brain tissue was isolated using TRIzol™ LS Reagent (#10296028; Invitrogen), followed by reverse transcription of RNA (1 µg) into complementary DNA (cDNA) by HiScript II reverse transcriptase (#R222; Vazyme Biotech). Then, the cDNA was used as a template for RT-qPCR assays using SYBR Green (#172-5125; BIO-RAD) according to the manufacturer's protocol. The procedure was performed as follows: heat activation of polymerase at 95°C for

10 min, followed by 45 cycles of 95°C for 15 s, 60°C for 15 s and 72°C for 20 s. The fluorescence was read and analyzed at 72°C. A final melting curve step from 55°C to 95°C was used to test the specificity of the primer. Ct values for the known concentrations of RNA were plotted against the logarithms of the genome equivalent copy numbers. The resultant standard curve was used to determine how many copies of ZIKV RNA genome equivalents were in the samples.²³ The specific primers used in RT-qPCR detection were as follows: ZIKV forward 5'-GGTCAGCGTCTCTAATAAACG-3', reverse 5'-GCACCCTAGTGTCCTTTCC-3'.

2.6 | Hematoxylin and eosin (HE) staining

Brain tissue was fixed in 4% paraformaldehyde fixation solution (#BL539A; Biosharp) for 48 h, routinely trimmed into standard cross-sections, and treated with paraffin. Then the slices were cut into 4 µm sections, mounted on 3-aminopropyltriethoxysilane-coated slides, and stained with HE to observe the inflammatory cell infiltration and necrosis in the hippocampus, thalamus, and cortical regions of the mouse brain. The slides were scanned by a Panoramic 250 Flash II Slide Scanner and photographs were taken with the 3DHISTECH panoramic slide viewer at magnifications of 100× and 200×.

2.7 | Immunofluorescence analysis of mouse brain

Paraffin sections of coronal brain tissue were subjected to immunofluorescence staining. Paraffin sections were deparaffinized in distilled water, repaired with ethylenediaminetetraacetic acid antigen retrieval solution (pH 8.0, #G1206; Servicebio), blocked with 3% BSA (#G5001; Servicebio) for 30 min, incubated with primary antibody overnight at 4°C, and then incubated with secondary antibody at room temperature in the dark for 50 min. After washing 3 times with PBS (#G002; Servicebio) for 5 min each time, the tissue was counterstained with DAPI solution (#G1012; Servicebio) and incubated for 10 min at room temperature in the dark. After washing again, an autofluorescence quencher (#G1401; Servicebio) was added for 5 min, and the section was rinsed with running water for 10 min, mounted, and observed under a microscope (Nikon Eclipse C1). The nuclei stained with DAPI were blue under ultraviolet light excitation, and the positive expression was the corresponding fluorescein-labeled green light. Primary antibodies included E antibody (1:100, #ab214333; Abcam) and NS1 antibody (1:100, #ab214337; Abcam).

2.8 | RNA extraction, library construction, and sequencing

Brain tissue was collected for RNA-seq analysis. According to the manufacturer's protocol, we extracted total RNA using the TRIzol™ LS Reagent. An Agilent 2100 Bioanalyzer (Agilent Technologies) was

used to assess the quality of the RNA, and RNase-free agarose gel electrophoresis was used to check it. The RNA integrity number (RIN) was used to evaluate the integrity of total RNA. Smaller values of RIN indicate more severe degradation, and 10 represents the highest integrity. When $RIN \geq 7$ and $28S/18S \geq 0.7$, the quality of the sample met the experimental requirements. When $RIN < 6$ or $28S/18S < 0.7$, the quality of the sample did not meet the experimental requirements. The cDNA fragments were purified with a QIAquick RT-qPCR extraction kit (Qiagen), end-repaired, poly(A)-tailed, and ligated to Illumina sequencing adapters, and an Illumina Novaseq 6000 instrument was used for sequencing by Gene Denovo Biotechnology Co.

2.9 | Data processing and bioinformatics analyses

Fastp (version 0.18.0)²⁴ software was used to filter the reads obtained by sequencing. The filtering criteria were as follows: (1) reads containing adapters were deleted; (2) reads containing more than 10% unknown nucleotides (N) were removed; and (3) low-quality reads containing more than 50% low-quality (Q value ≤ 20) bases were removed. The short-read alignment tool Bowtie2²⁵ (version 2.2.8) was used for mapping reads to the ribosome RNA (rRNA) database, and the mapped (rRNA) reads were then removed. The remaining clean reads were further used in assembly and gene abundance calculations. We mapped the clean paired-end reads to the reference genome using HISAT2. 2.4.²⁶ The setting “-rna-strandness RF” was used, and other parameters were set to the default values. StringTie v1.3.1²⁷ was used to assemble the mapped reads of each sample with a reference-based approach. StringTie software was used to calculate the FPKM (fragment per kilobase of transcript per million mapped reads) value of each gene to quantify its expression abundance and variations. The FPKM formula is shown as follows:

$$FPKM = \frac{10^6 C}{NL/10^3}$$

Based on the FPKM value of each gene, we show the expression distribution of different sample genes or transcripts through the expression distribution map. In addition, we used the R program (<http://www.r-project.org/>) to do principal component analysis (PCA) and calculate the Pearson correlation coefficient between samples to understand the repeatability between samples and to help exclude outlier samples. The DESeq²²⁸ package in R was used to screen the differentially expressed genes (DEGs) between the ZIKV-infected brain tissue and the control group. The parameters of false discovery rate (FDR) < 0.05 and absolute fold change (FC) > 2 were set as the screening criteria. Heatmaps and volcano maps were used to show the differences between the two groups.

2.10 | Gene Ontology (GO) and Kyoto Encyclopedia of Genes and Genomes (KEGG) enrichment analysis

All DEGs in ZIKV-infected mice were searched in the GO (<http://www.geneontology.org/>)²⁹ and KEGG (<https://www.genome.jp/kegg/>)³⁰ databases, and the number of genes annotated with each term was calculated.

2.11 | Identification of ferroptosis regulators in a ZIKV-infected mouse model

We performed gene set enrichment analysis (GSEA) using “GSEA” software (version: 4.2.3)³¹ and the “MSIGDB” database³¹ to determine whether genes in a specific KEGG pathway showed significant differences between ZIKV-infected mice and the control group, thus explaining the role of their regulation in the functional analysis.

The “ClueGO” plugin in Cytoscape software (Version: 3.9.1) was used for GO and KEGG enrichment analysis and visualization of ferroptosis regulators. The EVenn website (<http://www.ehbio.com/test/venn/#/>) was used to draw Venn diagrams. The “heatmap” package in R was used to draw heatmaps, the “corr” package was used to draw correlation network graphs, and the STRING (Version: 11.5, <https://cn.string-db.org/>) database was used to draw a protein-protein interaction network diagram.

2.12 | Screening, validation, and comprehensive analysis of ferroptosis regulators

2.12.1 | Compilation of other RNA-seq or experimental data

ZIKVID (<https://zikavid.org/database/>) database is intended to collect all information on gene expression changes caused by ZIKV infection in different host models, including their data sources, hosts, ZIKV strains and literature sources. The data are derived from published works in the PubMed database and include different methods for detecting and quantifying transcripts and proteins. A unique feature of this resource is that it provides not only high-throughput data from shotgun transcriptomics (such as RNA-Seq) or proteomics (such as MudPIT) but also individual gene expression measurements, such as from RT-qPCR or western blotting.

2.12.2 | Identification of immune cell type

The murine Microenvironment Cell Population counter (mMCP-counter), a method based on highly specific transcriptomic markers, was used to accurately quantify 16 immune and stromal murine cell

populations in R software,³² including T cells, CD8⁺ T cells, macrophages and monocytes, et al. Besides, Spearman's correlation analysis was conducted to determine whether the expression of ferroptosis regulators correlated with immune cell concentrations.

2.12.3 | RT-qPCR validation of RNA-seq data

RT-qPCR validations were conducted on ZIKV-infected ($n = 3$) and mock-infected brains ($n = 3$). Brain tissue was ground thoroughly in liquid nitrogen and then transferred to a 1.5-ml centrifuge tube, and 1 ml of TRIzol™ LS Reagent was added immediately to extract total RNA as described previously. Using the $2^{-\Delta\Delta CT}$ method, we measured relative messenger RNA (mRNA) expression levels in comparison to the β -actin housekeeping controls in RT-qPCR. The primer sequences used for RT-qPCR are listed in Table S1.

2.13 | Statistical analysis

Data are expressed as the mean \pm standard error of mean (SEM). The comparison between the two groups of data was performed using an unpaired the Student *t* test. GraphPad Prism v5, R software (Version: 4.6.1) and Cytoscape (Version 3.6.1) were used for visualization and statistical analyses.

3 | RESULTS

3.1 | ZIKV replicates in *IFNAR*^{-/-} mouse brain tissue and causes inflammatory pathology alterations

To evaluate whether ZIKV infection is pathogenic during brain development in mice, *IFNAR*^{-/-} mice were challenged with the 1×10^6 PFU of Asian ZIKV strain per mouse. There was no significant difference in the weight of the two groups of mice before model infection; with time went on, the weight of the control group showed an upward trend, and the weight of the ZIKV infection group showed a downward trend. On the ninth day, the mice were euthanized, and the difference in weight between the two groups was statistically significant (Figure 1A). Next, the viral RNA load in the brains of mice was determined by RT-qPCR, which showed that there was a significant difference in viral RNA load between the control and ZIKV groups (Figure 1B, $p < 0.0001$). Immunofluorescence staining of ZIKV-specific NS1 and E antibodies in mouse brain tissue showed that the fluorescence of both in the model group was significantly greater than that in the control group (Figure 1C).

To further investigate the possible pathogenic role of ZIKV infection in the brain, we also observed inflammatory and degenerative changes in the brain of *IFNAR*^{-/-} mice. In the ZIKV-infected group, HE staining showed varying degrees of infiltration of inflammatory cells (perivascular cuffing), vascular congestion or edema, nuclear pyknosis and neuronal vacuolization changes in the

hippocampus, thalamus, and cortex (Figure 2A,B). Together, our findings suggested that ZIKV infection leads to robust inflammatory brain damage in murine infections, which was consistent with the previous results of our research group.³³

3.2 | Transcriptomic landscape of the mouse brain after ZIKV infection

To explore the transcriptomic landscape of the mouse brain after ZIKV infection, a library of 6 cDNAs was generated by sequencing, and approximately 49 804, 573.33 (more than 99%) clean data on average were obtained for each sample. In addition, the base composition, quality, sequencing depth and other base information are presented in Table S2 and Table S3. A violin plot was used to identify groups that expressed different levels of genes (Figure S1A). The PCA plot was used to represent the samples in the ZIKV infection and control groups in a two-dimensional space (Figure S1B). The more similar the sample composition was, the closer samples were in the PCA plot. Pearson correlation analysis showed that the correlation coefficient squared (R²) between samples in the ZIKV group and control group was over 0.9 (Figure S1C). The sample cluster plot showed good separation between the two groups (Figure S1D). The above results met the requirements of our ensuing bioinformatics analysis.

A total of 3140 genes were identified as DEGs in the ZIKV group compared with the control group, including 2434 upregulated genes and 706 downregulated genes (Figure 3A, $|\log_2 FC| > 1$ and FDR < 0.05). Tables 1 and 2 report the 20 genes with the highest absolute values of $\log_2 FC$ and the corresponding adjusted *p* values. A complete list of DEGs can be found in Tables S4 and S5. A volcano map and heatmap were drawn to show the details of the DEGs (Figure 3B,C). We also plotted the top 20 genes for FC (Figure 3D) and verified the results of the top three genes in the RNA-seq FC ranking by RT-qPCR. These genes were Cxcl2 (FC = 27.1), Ifna4 (FC = 26.6), and Ifna2 (FC = 25.7) (Figure 3E). Our RNA sequencing data are mostly consistent with the RT-qPCR results, confirming their efficiency and reliability.

3.3 | Transcriptomic changes in mouse brain after ZIKV infection

Considering that the brain is one of the most important target organs of ZIKV infection, we used a hypergeometric test to find the entries that the DEGs mapped to in the GO and KEGG databases to understand the biological and overall transcriptional effects of ZIKV infection on brain tissue. GO includes three ontologies: biological process (BP), molecular function (MF), and cellular component (CC). Most of the entries in the GO analysis were related to immune responses. We examined the effects of ZIKV infection on the BPs, CCs and MFs of brain tissue. The highly activated BPs related to viral infection were "immune system process," "immune response," and

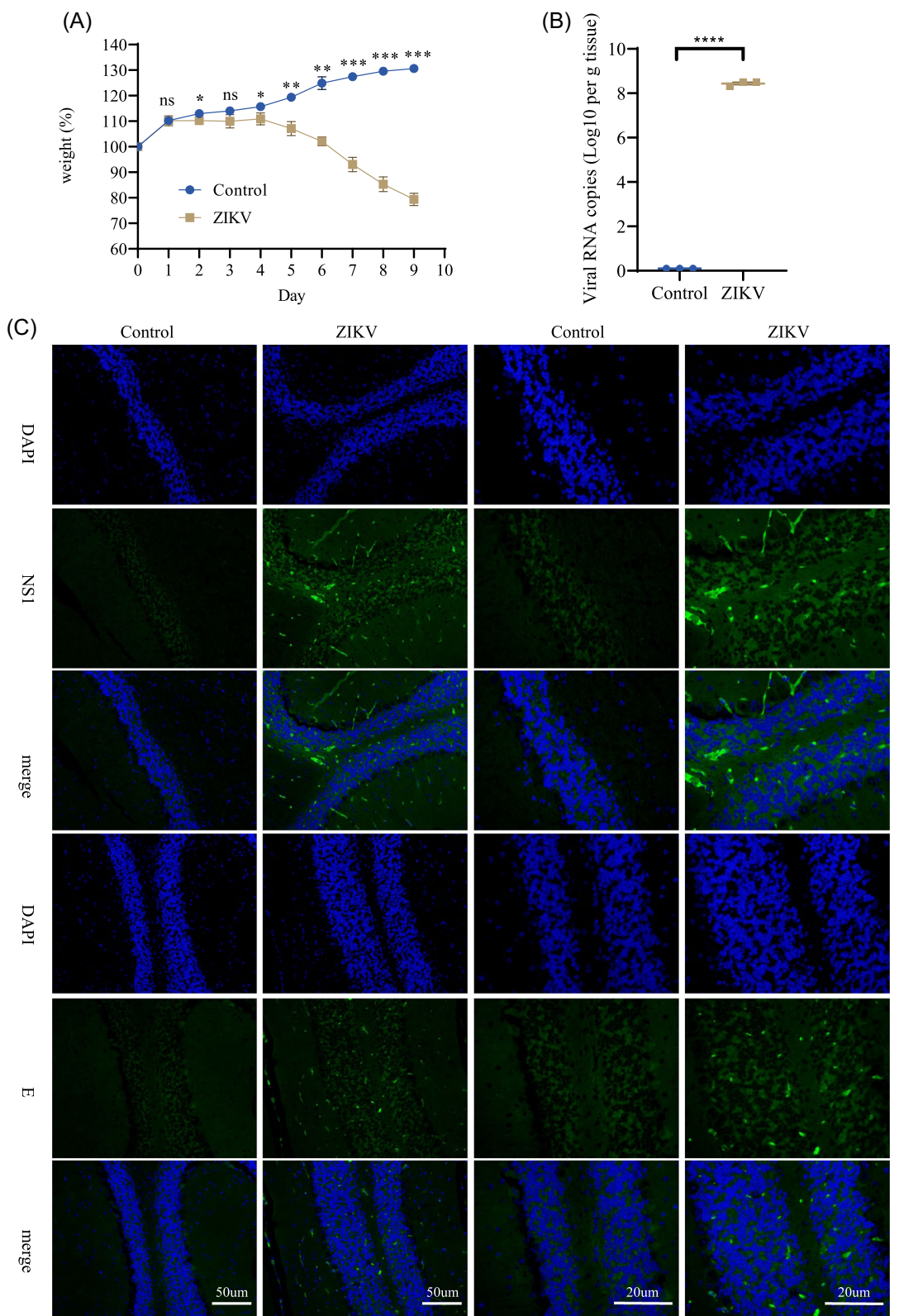


FIGURE 1 Replication of indicated viruses in *IFNAR^{-/-}* C57BL/6 mice ($n = 3$). Mice were infected with 1×10^6 PFU of the Asian ZIKV strain, or mock-infected. (A) Graph depicts body weight change of two groups. (B) Viral RNA load in brain tissue. Data were expressed as the mean \pm SEM. * $p < 0.05$, ** $p < 0.01$, *** $p < 0.001$, **** $p < 0.0001$. (C) Brain tissues were paraffin-embedded and processed, and then stained with antibodies against ZIKV-NS1 and ZIKV-E proteins. With the fluorescent secondary antibody, the NS1 and E proteins were detected in green, and the nuclei were stained with DAPI (in blue). ZIKV, Zika virus

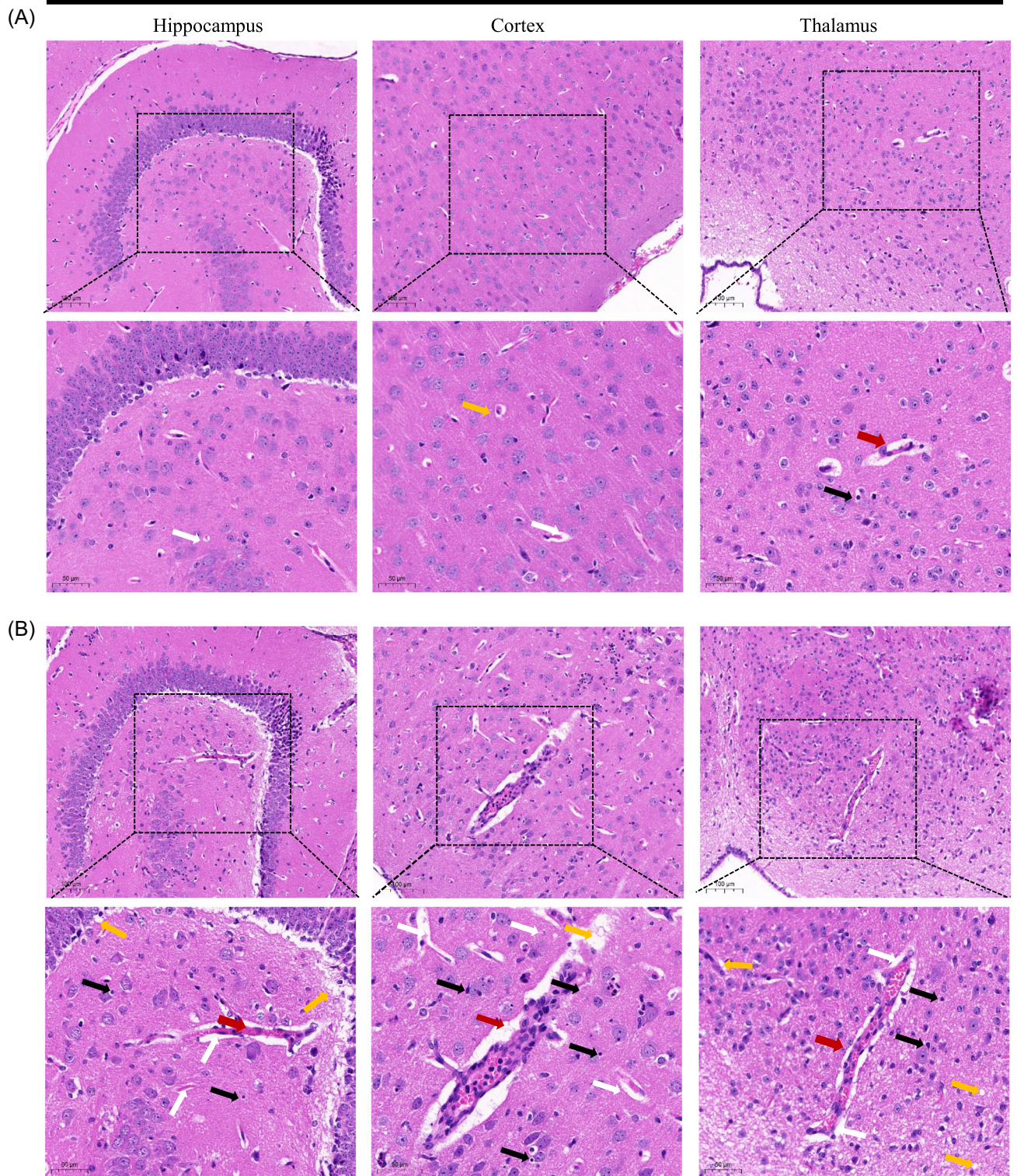
IFNAR^{-/-} C57BL/6 mice

FIGURE 2 HE staining of the brain tissue showed that ZIKV infection leads to alterations. Representative micrograph of the hippocampus, cortex, and thalamus in the mock-infected (A) ($n = 3$) and ZIKV-infected group (B) ($n = 3$). Scale bars, 100 mm (up) and 50 mm (down). Black arrows: nuclear pyknosis; red arrowheads: perivascular cuffing; orange arrows: neuronal vacuolization; white arrow: perivascular edema. HE, hematoxylin and eosin; ZIKV, Zika virus

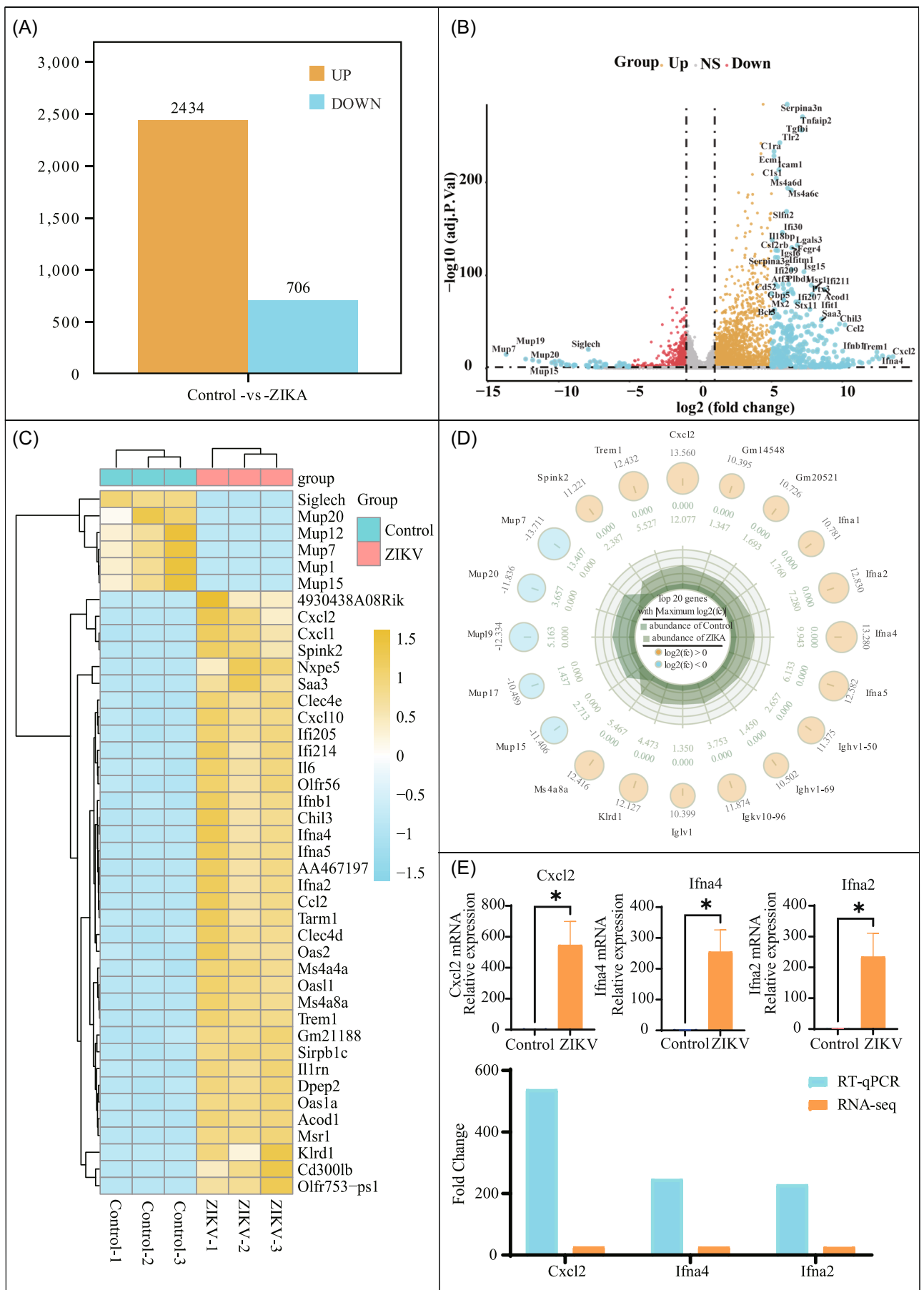
**FIGURE 3** (See caption on next page)

TABLE 1 Top 20 upregulated DEGs in ZIKV-infected mice brains

Symbol	Description	$\log_2(\text{FC})$	p-value	FDR
Cxcl2	Chemokine (C-X-C motif) ligand 2	13.55993468	2.85E-14	2.94E-13
Ifna4	Interferon alpha 4	13.27951386	9.58E-14	9.43E-13
Ifna2	Interferon alpha 2	12.82972274	2.63E-15	3.03E-14
Ifna5	Interferon alpha 5	12.58245565	6.82E-12	5.65E-11
Trem1	Triggering receptor expressed on myeloid cells 1	12.43219389	1.90E-19	3.07E-18
Ms4a8a	Membrane-spanning 4-domains, subfamily A, member 8A	12.41644569	1.57E-14	1.66E-13
Klrd1	Killer cell lectin-like receptor, subfamily D, member 1	12.12713455	1.90E-11	1.50E-10
Igkv10-96	Immunoglobulin kappa variable 10-96	11.87395671	5.04E-08	2.73E-07
Ighv1-50	Immunoglobulin heavy variable 1-50	11.37540151	5.12E-07	2.41E-06
Spink2	Serine peptidase inhibitor, Kazal type 2	11.22078137	2.60E-08	1.45E-07
Ifna1	Interferon alpha 1	10.78135971	7.38E-06	2.97E-05
Gm20521	Predicted gene 20521	10.72565028	6.78E-10	4.54E-09
Ighv1-69	Immunoglobulin heavy variable 1-69	10.50183718	1.99E-04	6.39E-04
Iglv1	Immunoglobulin lambda variable 1	10.39874369	1.65E-04	5.40E-04
Gm14548	Predicted gene 14548	10.39517708	2.50E-11	1.95E-10
Tff1	Trefoil factor 1	10.38082178	7.35E-06	2.96E-05
4930438A08Rik	RIKEN cDNA 4930438A08 gene	10.36632221	1.02E-09	6.66E-09
Ifna6	Interferon alpha 6	10.3553511	9.89E-06	3.92E-05
Igkv4-59	Immunoglobulin kappa variable 4-59	10.27224097	9.20E-04	2.63E-03
Ccl2	Chemokine (C-C motif) ligand 2	10.17893868	2.86E-49	1.72E-47

Abbreviations: cDNA, complementary DNA; DEG, differentially expressed genes; FDR, false discovery rate; ZIKV, Zika virus.

"defense response." In terms of CCs, the "extracellular region part," "extracellular region," and "cell surface" were most associated with ZIKV infection. Among MF terms, the DEGs were enriched in protein binding, signal receptor and cytokine functions. Most of these genes involved in regulating immune responses were upregulated (Figure 4A and Table S6).

KEGG analysis showed that the most significant entries in the brain tissue after ZIKV infection were closely related to the response between the virus and the body's cells and cytokines, such as

"Cytokine-cytokine receptor interaction," "Osteoclast differentiation," and "Viral protein interaction with cytokine and cytokine receptor" (Figure 4B and Table S7). Further analysis by GSEA showed that "TNF signaling pathway," "NOD-like receptor (NLR) signaling pathway," and "Toll-like receptor (TLR) signaling pathway" were significantly upregulated in brain tissue (Table S8). Notably, cell death-related categories such as "Apoptosis," "Necroptosis," "p53 signaling pathway," "Cellular senescence," "Cell cycle," "Apoptosis—multiple species," and "Ferroptosis" were also significantly enriched.

FIGURE 3 Transcriptomic analyses of ZIKV-infected mice and healthy controls. (A) The number of differentially expressed genes (DEGs) between two groups, in which orange represents upregulated genes and blue represents downregulated genes. (B) Volcano plot of DEGs between two groups. Orange represents upregulated genes, red represents downregulated genes, and grey indicates genes with no significant difference. Blue dots represent most significant DEGs ($|\log_2 \text{FC}| > 5$, FDR < 0.05). (C) Heatmap of DEGs ($|\log_2 \text{FC}| > 8$, FDR < 0.05) between two groups. (D) Radar chart showing the top 20 DEGs information that differs most between the two groups based on the $|\log_2 \text{FC}|$ value. (E) Relative expression levels of Cxcl2, Ifna4, and Ifna2 were measured in comparison to the β -actin housekeeping controls using the $2^{-\Delta\Delta CT}$ method (up) in mice brains ($n = 3$). Data are presented as mean \pm SEM. * $p < 0.05$. An analysis of the relative FC between RNA-Seq and RT-qPCR results (down). FC, fold change; FDR, false discovery rate; ZIKV, Zika virus

TABLE 2 Top 20 downregulated DEGs in ZIKV-infected mice brains

Symbol	Description	log ₂ (FC)	p-value	FDR
Mup7	Major urinary protein 7	-13.71066296	7.84E-17	1.05E-15
Mup19	Major urinary protein 19	-12.33408702	1.22E-11	9.84E-11
Mup20	Major urinary protein 20	-11.8363134	1.80E-10	1.29E-09
Mup15	Major urinary protein 15	-11.40585058	5.85E-09	3.49E-08
Mup17	Major urinary protein 17	-10.48850965	1.64E-07	8.29E-07
Serpina1e	Serine (or cysteine) peptidase inhibitor, clade A, member 1E	-10.28424575	4.03E-09	2.46E-08
Mup16	Major urinary protein 16	-10.22078137	1.25E-05	4.88E-05
Lenep	Lens epithelial protein	-9.960967268	2.22E-09	1.39E-08
Sult2a8	Sulfotransferase family 2A, dehydroepiandrosterone (DHEA)-preferring, member 8	-9.834997677	2.32E-05	8.68E-05
Mup18	Major urinary protein 18	-9.756973226	1.26E-07	6.44E-07
Mettl7b	Methyltransferase like 7B	-9.451211112	3.49E-05	1.27E-04
Aadac	Arylacetamide deacetylase	-9.451211112	7.89E-05	2.72E-04
Mup1	Major urinary protein 1	-9.283860054	6.81E-05	2.37E-04
C9	Complement component 9	-8.936637939	8.30E-05	2.85E-04
Hsd3b5	Hydroxy-delta-5-steroid dehydrogenase, 3 beta- and steroid delta-isomerase 5	-8.936637939	6.18E-04	1.83E-03
Ces3b	Carboxylesterase 3B	-8.886712714	7.23E-05	2.51E-04
Cyp1a2	Cytochrome P450, family 1, subfamily a, polypeptide 2	-8.834997677	1.20E-04	4.00E-04
Gm49027	Predicted gene, 49027	-8.058893689	1.78E-04	5.77E-04
Ugt3a2	UDP glycosyltransferases 3 family, polypeptide A2	-7.965784285	3.53E-04	1.09E-03
Dnase1	Deoxyribonuclease I	-7.926790153	1.54E-02	3.38E-02

Abbreviations: DEG, differentially expressed genes; FDR, false discovery rate; ZIKV, Zika virus.

3.4 | Identification of 12 ferroptosis-related signatures

Figure 5A provides a brief overview of the data of 12 key ferroptosis regulators in ZIKV-infected brain tissue. GSEA showed that both cell growth- and death-related pathways were activated in ZKIV-infected brain tissue (Figure 5B), but activation of ferroptosis in ZLKIV, a mode of cell death not reported in ZIKV, was of particular interest to us (Figure 5C). We performed Student's unpaired t test on 43 genes related to ferroptosis in GSEA, and the results showed that 25 genes were differentially expressed between the ZIKV-infected group and the control group (Figure S2). Therefore, we assessed the BPs and enriched pathways that these 25 ferroptosis regulators participate in. Our research revealed that "transition metal ion homeostasis," "iron ion transport," "iron ion transport," "cellular iron ion homeostasis," "transition metal ion transport," and "cellular transition metal ion homeostasis" were the most enriched BPs (Table S9). A total of 24 of the 25 genes were significantly enriched in ferroptosis, mineral

absorption, fatty acid biosynthesis, fatty acid degradation, the PPAR signaling pathway, peroxidase and adipokine signaling (Figure 5D and Table S10).

To increase the reliability of the data on ferroptosis regulators in ZIKV-infected model mice, we merged the DEGs and ferroptosis-related genes in the Ferrdb and GeneCards databases (Figure 5E). This yielded 12 ferroptosis regulators, including 11 DEGs that were upregulated in ZIKV infection, CYBB, HMOX1, CP, SAT1, TF, SLC39A14, FTL, LPCAT3, FTH1, SLC3A2, and TP53; SLC40A1 was the only DEG downregulated in ZIKV-infected brain tissue. We displayed the FPKM levels of these 12 genes in a heat map (Figure 5F). The correlation network map showed that SLC40A1 was strongly negatively correlated with the remaining 11 genes (Figure 5G). The protein-protein interaction network showed that these 12 ferroptosis regulators can interact in seven ways, including experiments, coexpression, neighborhood, text mining, databases, gene fusion, and cooccurrence (Figure 5H).

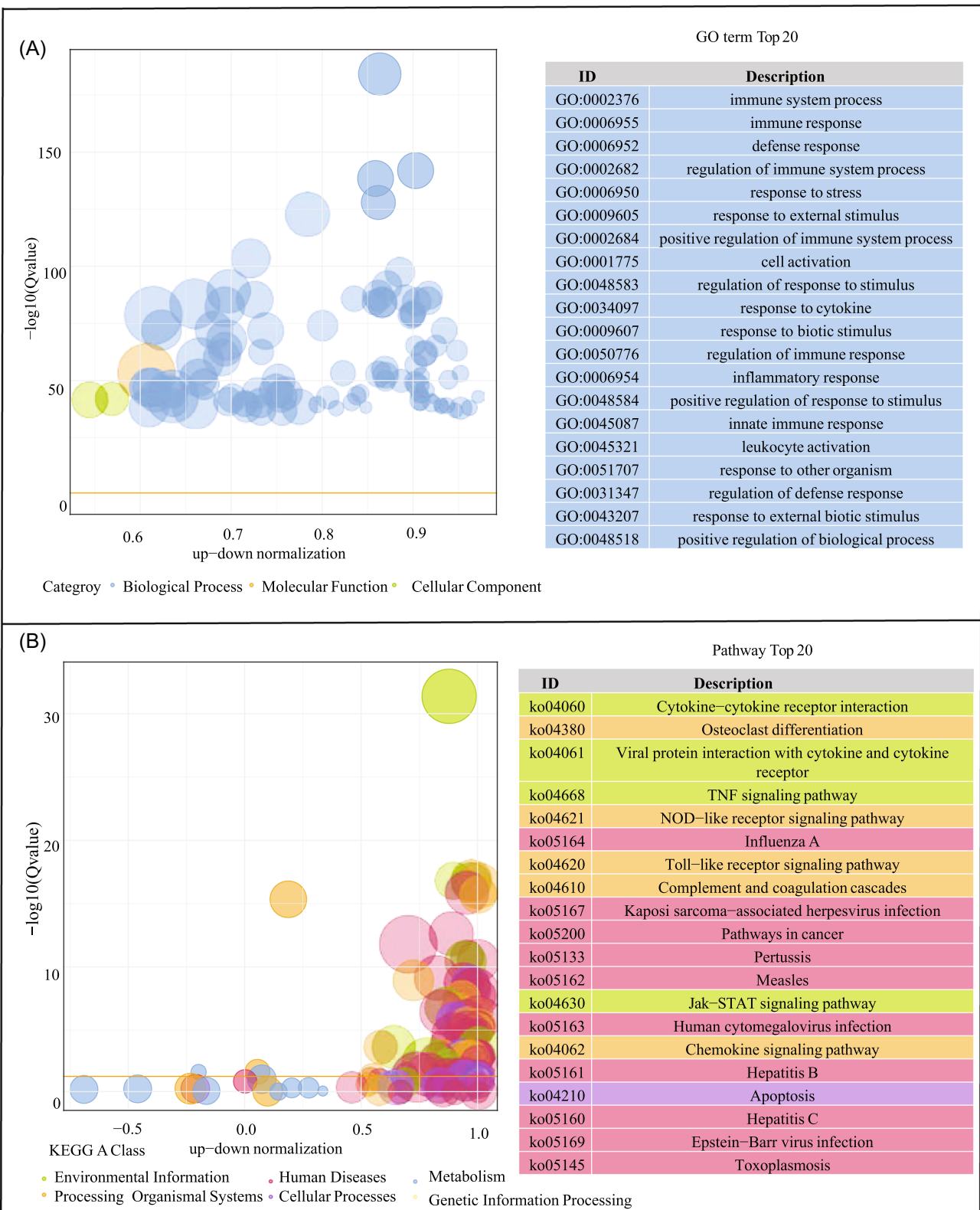


FIGURE 4 Bubble plots of Gene Ontology (GO) (A) and Kyoto Encyclopedia of Genes and Genomes (KEGG) (B) of significantly differentially expressed genes between ZIKV-infected mice and healthy controls. ZIKV, Zika virus.

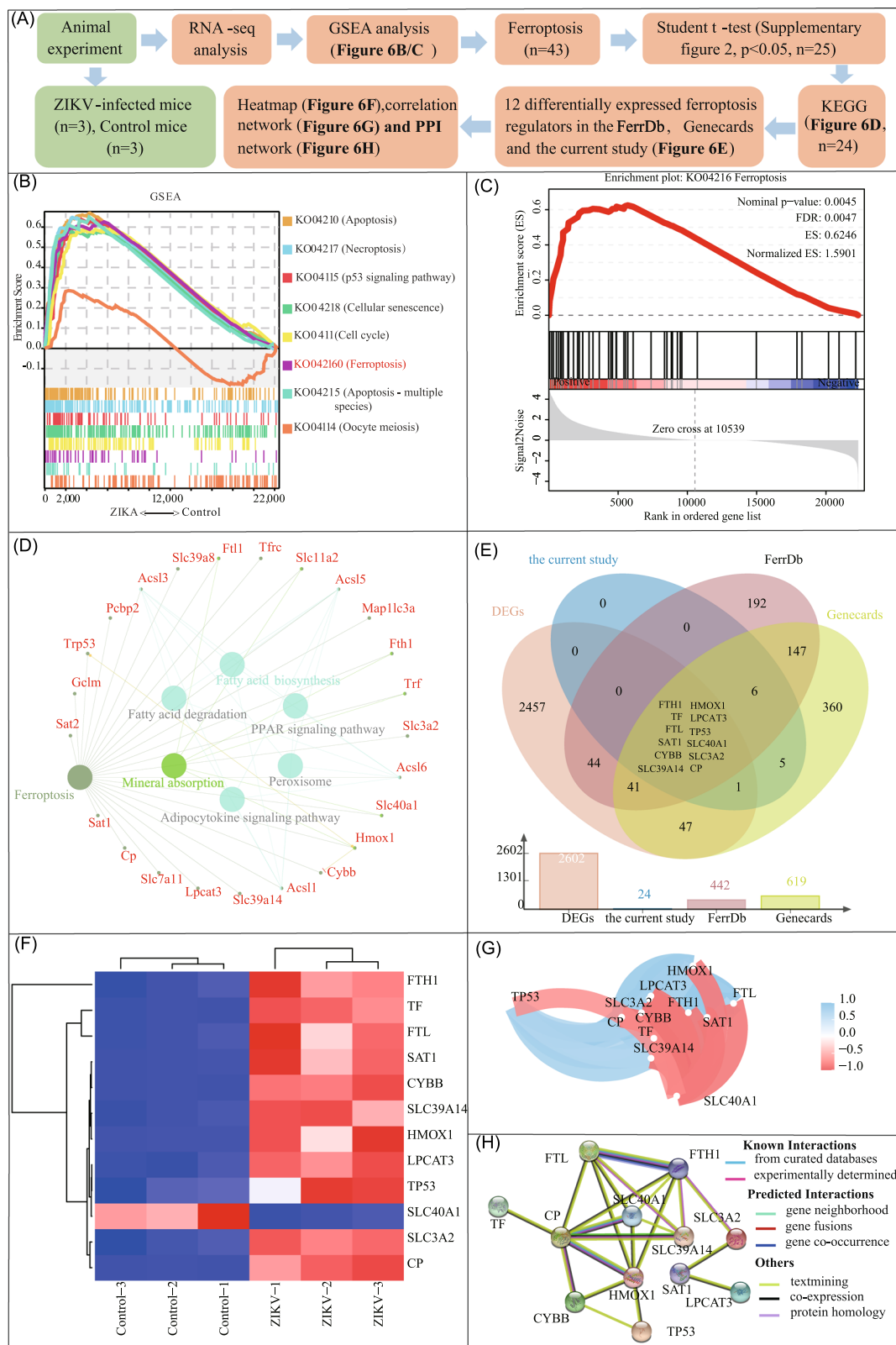


FIGURE 5 Bioinformatics methods to identify a series of ferroptosis regulators in ZIKV infected mice. (A) Experimental scheme to identify ferroptosis-related regulators; (B) Gene set enrichment analysis (GSEA) for the cell growth and death related pathways; (C) GSEA for the ferroptosis-related pathway; (D) Kyoto Encyclopedia of Genes and Genomes enrichment analysis network diagram of ferroptosis-related genes. (E) Venn diagram of humanized DEGs, ferroptosis regulators in the current study, ferroptosis genes in the FerrDb and Genecards databases between two groups. (F) Heatmap representing the expression levels of 12 hub ferroptosis genes in ZIKV-infected mice. Blue indicates low expression; red indicates high expression. The deeper the color, the higher the expression value. (G) Network correlation map showing the 12 ferroptosis genes in ZIKV-infected mice. The blue color indicates negative correlations, while the red color indicates positive correlations. (H) Protein-protein interaction networks of 12 hub ferroptosis genes in ZIKV-infected mice. Different colors represent different modes of interactions. ZIKV, Zika virus.

3.5 | Comprehensive analysis of 12 ferroptosis-related signatures associated with ZIKV infection

To systematically study 12 ferroptosis regulators related to ZIKV infection, we obtained basic information on the ZIKVID database. All 12 ferroptosis regulators except CP were reported in PubMed and are expressed differently in vitro between the ZIKV infection and mock infection groups, consistent with our study. In general, we have demonstrated the accuracy and reliability of our RNA sequencing data through multiple experimental methods and through verification by others (Table 3).

Since ferroptosis is closely associated with immunity, we examined the differences in immune infiltration between the ZIKV and control groups. Based on the mMCP-counter method, we quantified the immune cells and stromal cells in the brain tissue of the ZIKV and control groups and further compared the degree of infiltration of 16 types of immune cells and stromal cells between the two groups (Figure 6A). Figure 6B shows that CD8⁺ T cells, monocytes, B-derived cells, macrophages, neutrophils, vessels and fibroblasts infiltrated more in the ZIKV group ($p < 0.05$), and we observed the opposite trend in lymphocytes and eosinophils, further suggesting the importance of the immune process in ZIKV-infected brain tissue.

Then, we evaluated the relationship between 12 ferroptosis regulators and crucial immune cell populations in ZIKV infection (CD8⁺ T cells, macrophages, monocytes and B cells). HMOX1 showed the strongest positive correlation with CD8⁺ T cells ($r = 0.96$, $p = 0.0026$) and macrophages ($r = 0.99$, $p = 7.07E-05$). There was a negative correlation between SLC40A1 and B cells ($r = -0.92$, $p = 0.010$), monocytes ($r = -0.93$, $p = 0.0073$), and macrophages ($r = -0.92$, $p = 0.010$). A negative correlation was found between monocytes ($r = 0.97$, $p = 0.00099$) and SAT1, and strong positive associations were found between CYBB and B cells ($r = 0.99$, $p = 9.32E-05$) and macrophages ($r = 0.97$, $p = 0.00025$) (Figure 6C). Hence, HMOX1, SLC40A1, CYBB, and SAT1 were considered crucial ferroptosis regulators in ZIKV infection (Table S11).

Finally, in *IFNAR^{-/-}* C57BL/6 mice, we further validated the mRNA expression of CYBB, SAT1, SLC40A1 and HMOX1, as seen from the RNA-seq transcriptome profiling, by RT-qPCR on ZIKV-infected and control brain tissue. RT-qPCR showed statistically significant differences between the two groups. *Slc40a1* had low expression in the control group, while *Cybb*, *Hmox1*, and *Sat1* were significantly upregulated in the ZIKV-infected group (Figure 6D).

4 | DISCUSSION

Here we described neuropathological changes in the brain tissue of ZIKV-infected mice and provided relevant evidence. Furthermore, we proposed that this impairment in brain may be related to ferroptosis based on our RNA-seq data. Ferroptosis genes were shown to be highly correlated with the expression of macrophages, monocytes,

CD8⁺ T cells, and B-derived cells. For the first time, our team identified the significant value of ferroptosis in ZIKV infection, which may provide a foundation for studying the neuroinflammatory mechanism of ZIKV disease and facilitate the development of an anti-ZIKV strategy.

ZIKV is a pathogenic neurotropic virus that crosses the blood-brain barrier, infects the CNS of adults, and causes various neurological complications.³⁴ ZIKV has been detected in the brains and CSF of adults.^{10,35} In adult mice, ZIKV preferentially targets memory-related brain regions, inhibits hippocampal long-term potentiation, and induces memory impairment.³⁶ ZIKV can infect the hypothalamus, resulting in delayed growth and development as well as impaired memory and learning in mice.³⁷ A case report also reported neuropsychological and cognitive changes in an adolescent following ZIKV infection.³⁸ However, the mechanisms responsible for infecting mature CNS remain unclear. The *IFNAR^{-/-}* mouse is susceptible to lethal ZIKV infection and has previously been used as a small animal model of the pathogenesis of flaviviruses, such as DENV and YFV.^{39,40} Based on previous research, our team established a ZIKV-infected *IFNAR^{-/-}* mouse model by intraperitoneal injection of 1×10^6 PFU ZIKV virus into adult mice.^{33,41} While fever and general discomfort are typical features of human ZIKV infection, similar observations were not observed in our ZIKV-infected mice. In our experiment, on the fourth to fifth day after ZIKV challenge, the mice in the model group showed symptoms of different severity, such as decreased activity, weight loss and worsening of the disease. On Day 9, the weight of the mice dropped to near the humanitarian endpoint. Then, brain tissue from ZIKV-infected mice was used for pathological observation and viral quantification. HE staining showed varying degrees of infiltration of inflammatory cells (perivascular cuffing), vascular congestion or edema, nuclear pyknosis and neuronal vacuolization changes in the hippocampus, thalamus, and cortex. Quantitative analysis of viral load by RT-qPCR and immunofluorescence staining indicated that ZIKV did infect brain tissue. Hence, our *IFNAR^{-/-}* mouse model is suitable for studying ZIKV infection.

To further monitor ZIKV infection-induced transcriptome alterations in mice, RNA-seq was performed. At present, high-throughput next-generation sequencing technology is considered to be the gold standard for clinical genetic diagnosis, and its diagnostic capability and accuracy have been continuously improved.⁴² In our study, RNA-seq of brain tissue identified 3140 DEGs in ZIKV-infected mice, including 2434 upregulated DEGs and 706 downregulated DEGs in the ZIKV group. The results of GO enrichment analysis of the DEGs showed that the DEGs were significantly enriched in multiple BPs, such as immune system processes, immune response, defense response and regulation of immune system processes. At the same time, these DEGs were enriched in MFs related to binding to various proteins, signal receptors and cytokines. In KEGG enrichment analysis, cytokine–cytokine receptor interactions, osteoclast differentiation, viral protein interactions with cytokines and cytokine receptors, and the TNF signaling pathway also showed close relationships with ZIKV infection. The innate immune system

TABLE 3 Basic information of key ferroptosis regulators in ZIKV-infected mice

Gene symbol	Human symbol	Description	Host	Strain	Method	Expression	PMID
Cybb	CYBB	Cytochrome b-245, beta polypeptide	in vitro—Human neural progenitor cells (hNPCs)	African ZIKV	RNA-seq	Up	27729407
Hmox1	HMOX1	Heme oxygenase 1	in vitro—Human neural progenitor cells (hNPCs)	African ZIKV and Asian ZIKV	RNA-seq	Up	27580721
Cp	CP	Ceruloplasmin					
Sat1	SAT1	Spermidine/spermine N1-acetyl transferase 1	in vitro—Human neural progenitor cells (hNPCs)	African ZIKV (MR766)	RNA-seq	Up	26952870
Trf	TF	transferrin	in vitro—Human Mesenchymal Stem Cells (hMSC)	Brazilian ZIKV	Proteomics	Down	30377986
Slc39a14	SLC39A14	Solute carrier family 39 (zinc transporter), member 14	in vitro—Human primary retinal pigmented epithelial (RPE) cells	American ZIKV (Strain PRVABC59)	RNA-Seq	Up	30046058
Slc39a14	SLC39A14	Solute carrier family 39 (zinc transporter), member 14	in vitro—Human neural progenitor cells (hNPCs)	African ZIKV (MR766)	RNA-seq	Up	26952870
Slc39a14	SLC39A14	Solute carrier family 39 (zinc transporter), member 14	in vitro—Human Mesenchymal Stem Cells (hMSC)	Brazilian ZIKV	Proteomics	Up	30377986
Slc39a14	SLC39A14	Solute carrier family 39 (zinc transporter), member 14	in vitro—Human neural progenitor cells (hNPCs)	ZIKV (S/MGCG-1 strain accession number KX266255)	Proteomics (LC-MS/MS Analysis)	Up	29922247
Slc39a14	SLC39A14	Solute carrier family 39 (zinc transporter), member 14	in vitro—Human Neural Stem Cells (hNSCs)	Asian ZIKV	RNA-seq	Up	28216147
Slc39a14	SLC39A14	Solute carrier family 39 (zinc transporter), member 14	in vitro—Human neural progenitor cells (hNPCs)	African ZIKV (MR766)	RNA-seq	Down	29116029
Ftl1	FTL	Ferritin light polypeptide 1	in vitro—Human neural progenitor cells (hNPCs)	African ZIKV (MR766)	RNA-seq	Up	26952870
Ftl1	FTL	Ferritin light polypeptide 1	in vitro—Human Mesenchymal Stem Cells (hMSC)	Brazilian ZIKV	Proteomics	Up	30377986
Lpcat3	LPCAT3	Lysophosphatidylcholine acyltransferase 3	in vitro—Human neural progenitor cells (hNPCs)	African ZIKV (MR766)	RNA-seq	Up	26952870
Fth1	FTH1	Ferritin heavy polypeptide 1	in vitro—Human Mesenchymal Stem Cells (hMSC)	Brazilian ZIKV	Proteomics	Up	30377986
Slc3a2	SLC3A2	Solute carrier family 3 (activators of dibasic and neutral amino acid transport), member 2	in vitro—Human neural progenitor cells (hNPCs)	African ZIKV (MR766)	RNA-seq	Up	26952870

TABLE 3 (Continued)

Gene symbol	Human symbol	Description	Host	Strain	Method	Expression	PMID
Slc3a2	SLC3A2	Solute carrier family 3 (activators of dibasic and neutral amino acid transport), member 2	in vitro—Human neural progenitor cells (hNPCs)	ZIKV (SMGC-1 strain accession number KX266255)	Proteomics (LC-MS/MS Analysis)	up	29922247
Slc3a2	SLC3A2	Solute carrier family 3 (activators of dibasic and neutral amino acid transport), member 2	in vitro—Human Neural Stem Cells (hNSCs)	Asian ZIKV	RNA-seq	Up	28216147
Slc3a2	SLC3A2	Solute carrier family 3 (activators of dibasic and neutral amino acid transport), member 2	in vitro—Human neural progenitor cells (hNPCs)	African ZIKV and Asian ZIKV	RNA-seq	Up	27580721
Slc3a2	SLC3A2	Solute carrier family 3 (activators of dibasic and neutral amino acid transport), member 2	in vitro—Human neural progenitor cells (hNPCs)	African ZIKV (MR766)	RNA-seq	Down	29116029
Trp53	TP53	Transformation related protein 53	in vitro—Human neural progenitor cells (hNPCs)	ZIKV (SMGC-1 strain accession number KX266255)	Proteomics (LC-MS/MS Analysis)	up	29922247
Trp53	TP53	Transformation related protein 53	in vitro—Human neural progenitor cells (hNPCs)	African ZIKV (MR766)	RNA-seq	Down	29116029
Trp53	TP53	Transformation related protein 53	in vitro—Human neural progenitor cells (hNPCs)	African ZIKV and Asian ZIKV	RNA-seq	Up	27580721
Trp53	TP53	Transformation related protein 53	in vitro—Human neural progenitor cells (hNPCs)	African ZIKV (MR766)	RNA-seq	Up	26952870
Slc40a1	SLC40A1	Solute carrier family 40 (iron-regulated transporter), member 1	in vitro—Human Neural Stem Cells (hNSCs)	Asian ZIKV	RNA-seq	Down	28216147

Abbreviation: ZIKV, Zika virus.

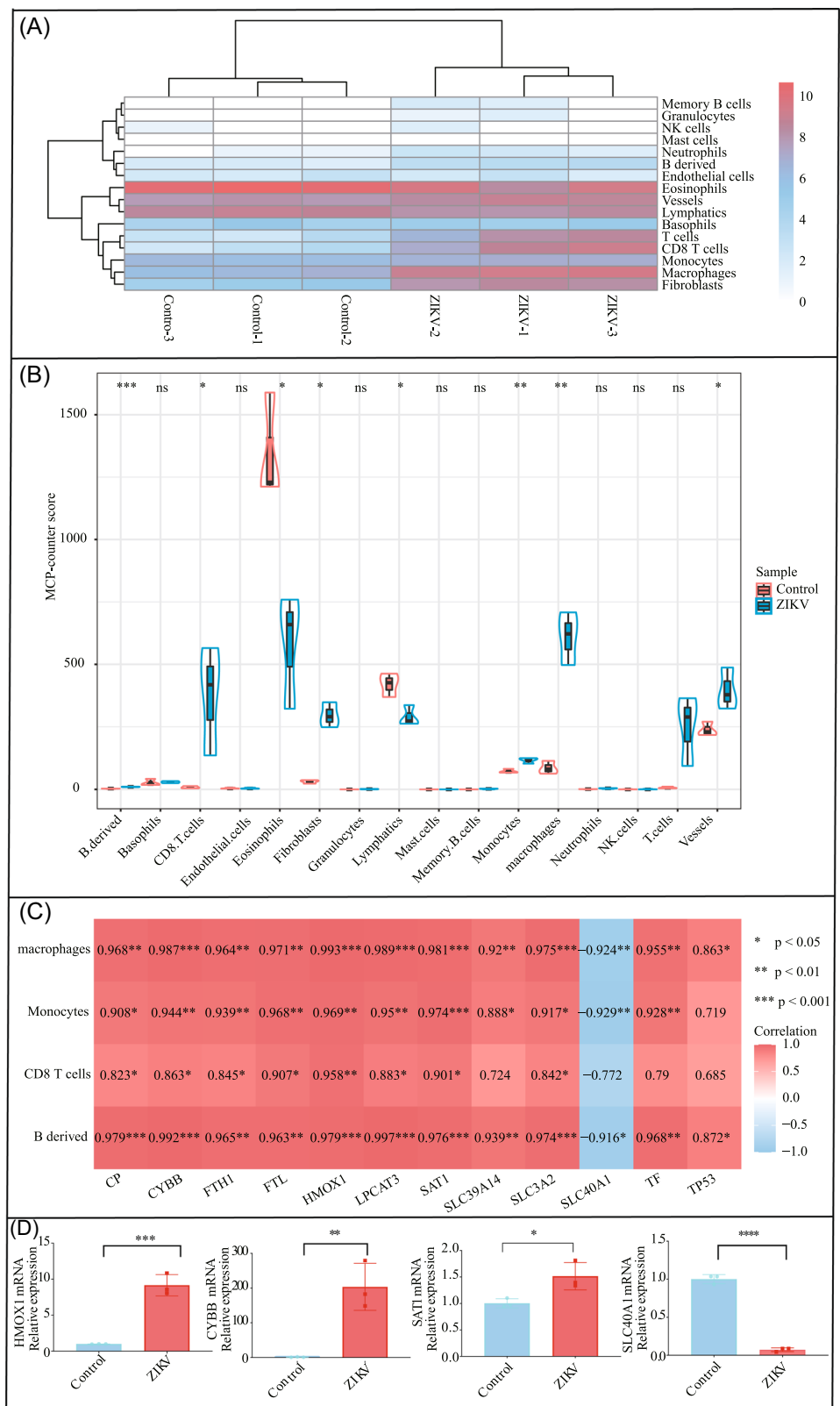


FIGURE 6 Profiles of immune cells infiltration in mice between two groups. (A) Heatmaps showing the infiltrating abundance of 14 immune cells and 2 stromal cells based on the R-package of MCP-counter. (B) Violin plot showing the differential expression of 14 immune cells and 2 stromal cells between two groups based on mMCP-counter scores. (C) Heat map showing the correlation between 12 ferroptosis regulators and macrophages, monocytes, CD8⁺ T cells, and B-derived cells. (D) RT-qPCR analysis of the relative mRNA expression of HMOX1, CYBB, SAT1, and SLC40A1 between two groups. The level of mRNA expression was normalized to the β -actin housekeeping controls. Data was shown as mean \pm SEM, *p < 0.05; **p < 0.01, ***p < 0.001, ****p < 0.0001, ns, not significant (two-tailed unpaired the Student t test). mRNA, messenger RNA.

antagonizes ZIKV replication by producing interferon (IFN) and IFN-stimulated gene-related proteins.⁴³ As the host's first line of defense against infection, the innate immune system has multiple pattern recognition ligands, such as TLRs and NLRs, that activate immune cells by recognizing different viral and microbial components.⁴⁴ In adaptive immunity, ZIKV infection has been shown to induce T-cell activation in both human and mouse models, but T cells play a role in limiting ZIKV infection only when type I IFN responses are impaired.⁴⁵ Kellie A. Jurado et al.⁴⁶ show that an increased number of Foxp3+ regulatory T cells were found in ZIKV-infected compared to mock-infected *IFNAR1^{-/-}* mice, further illustrating the importance of adaptive immunity in the ZIKV response. A recent study by Noreen Mumtaz et al.⁴⁷ show that ZIKV infection disrupts osteoclast differentiation and function, and speculated that ZIKV-associated microcephaly may be involved. Claudia P. Figueiredo et al.³⁶ report that ZIKV replication and TNF- α upregulation in adult brain tissue may induce synaptic and memory dysfunction.

Ferroptosis, a nonapoptotic iron-dependent cell death method. The process of ferroptosis is characterized by an abundance of intracellular lipid reactive oxygen species (ROS), which cause the oxidation of lipids, leading to cell death and cell membrane injury.^{48,49} In our study, ferroptosis was activated in the ZIKV infection group, and 43 ferroptosis regulators were enriched. Our research revealed that "transition metal ion homeostasis," "iron ion transport," "iron ion transport," "cellular iron ion homeostasis," "transition metal ion transport," and "cellular transition metal ion homeostasis" were the most enriched BPs. KEGG of ferroptosis regulators revealed their involvement in pathways such as mineral absorption, fatty acid biosynthesis, fatty acid degradation, PPAR signaling pathway, peroxidase and adipokinesine signalling pathway. PPARy is a major regulator of cell cycle, metabolism, lipogenesis, and inflammation. The link between inflammation and neurodegeneration in the brain has been extensively studied.⁵⁰ An RNA-seq data from neurons derived from human-induced pluripotent stem cells infected by ZIKV reveals the imbalance of the "PPAR signal pathway" at the transcriptome level.⁵¹ Finally, we identified 12 key ferroptosis regulators in brain tissues infected by ZIKV, including 11 upregulated ferroptosis regulators (CYBB, HMOX1, CP, SAT1, TF, SLC39A14, FTL, LPCAT3, FTH1, SLC3A2, and TP53) and one downregulated (SLC40A1) ferroptosis gene in the ZIKV infection group.

Ferroptosis can release and activate damage-associated molecular patterns or lipid oxidation products to be sensed by immune cells through distinct intracellular signal transduction pathways, resulting in distinct immune and inflammatory responses.⁵² In our study, we analyzed the correlation between immune cell infiltration proportions and ZIKV infection and the correlation between ferroptosis-related genes and immune cells. The findings indicated that CD8 $^{+}$ T cells, B-derived cells, macrophages, monocytes had high level of immune cell infiltration in the ZIKV-infected group. HMOX1, SAT1, SLC40A1, and CYBB displayed the highest correlation with major immune cells such as CD8 $^{+}$ T cells, B-derived cells, macrophages and monocytes. T-cell activation is redox dependent, T-cell receptor stimulation induces ROS production, and mitochondrial ROS are critical for T-cell

activation and expansion.^{53,54} The CD8 $^{+}$ T cells in flaviviruses, including ZIKV, may play a dual role. Annie Elong Ngono et al.⁵⁵ revealed the protective role of CD8 $^{+}$ T cells in ZIKV infection. Huarong Huang et al.⁵⁶ reported strong CD8 $^{+}$ T cell responses in ZIKV infected mice; When ZIKV infects CNS, an amount of virus specific CD8 $^{+}$ T cells are recruited in brain tissue. In the brain, microglia, or resident macrophages, protect the brain against infection and injury⁵⁷ and play an important physiological role in iron metabolism and circulation.⁵⁸ Therefore, HMOX1, CYBB, SAT1 and SLC40A1 were identified as key ferroptosis regulators in the mechanism of ZIKV infection.

HMOX1, also known as HO-1, catalyzes the conversion of heme to ferrous iron and biliverdin.⁵⁹ Chang et al.⁶⁰ showed that BAY (IkB inhibitor) induces ferroptosis through the Nrf2-SLC7A11-HO-1 pathway, in which HO-1 is a key mediator in response to a cellular redox state. In another study, HO-1 was shown to be an antiferroptosis factor that protects against kidney injury.⁶¹ Thus, HO-1 regulates ferroptosis in a complex manner. In our study, HO-1 was upregulated more than eightfold in the ZIKV group, and its high expression status in the model group and its diagnostic performance were also validated in ZIKV-infected brain glial cells in vitro. SAT1 is a rate-limiting enzyme in polyamine catabolism critically involved in the conversion of spermidine and spermine back to putrescine. SAT1, a target gene of p53, has been shown to activate ferroptosis. When SAT1 expression is activated, lipid peroxidation occurs, which increases cell vulnerability to ferroptosis and suppresses their response to reactive oxygen species (ROS)-induced stress.⁶² Solute carrier family 40 member 1 (SLC40A1), also known as FPN1, is the only iron export protein discovered in mammals, and inhibition of it induces ferroptosis.⁶³ It has been demonstrated that dapagliflozin (DAPA) improves ferroptosis during diabetic renal tubular injury by stabilizing SLC40A1.⁶⁴ The NADPH oxidase CYBB (Nox2) is present in the cellular walls of all vascular walls, and NADPH oxidases (Nox) are the main sources of ROS in the vascular system.⁶⁵

Collectively, we identified a link between ferroptosis regulators and ZIKV infection via RNA-seq technology for the first time. Through RNA-seq analysis of ZIKV-infected brain tissue, we found that the ferroptosis pathway was activated and contributed to or inhibited the expression of related ferroptosis regulators during infection, suggesting that ferroptosis might play a critical role in ZIKV infection. We further quantified differentially expressed immune cells between ZIKV and controls, finding that CD8 $^{+}$ T cells, macrophages, and monocytes were upregulated in terms of their proportions in ZIKV infection and were significantly associated with ferroptosis regulators such as CYBB, HMOX1, SLC40A1, and SAT1. Finally, we validated the differential expression of these 4 keys immune-related ferroptosis regulators CYBB, HMOX1, SLC40A1, and SAT1 in ZIKV-infected and control mice by RT-qPCR, and these findings were further supported by several human vitro experiments.

This study based on functional analysis of RNA-seq data has certain limitations. We only proposed the possible mechanism of ferroptosis in ZIKV infection, and the research on ferroptosis and

immune cell infiltration is also in the preliminary stage. The underlying mechanism to explain how ferroptosis affects ZIKV infection in vivo remains unclear. Studies are needed to confirm the results of this study in the future, which would provide essential insights into the mechanism of ZIKV infection and the resulting neuronal cell death.

AUTHOR CONTRIBUTIONS

Conceptualization: Zizhao Lao; Qian Yan; Wengjiang Zheng; Shaofeng Zhan; Xiaohong Liu. **Data curation:** Qian Yan; Wenjiang Zheng. **Formal analysis:** Zizhao Lao; Qian Yan; Wengjiang Zheng. **Funding acquisition:** Xiaohong Liu; Geng Li. **Investigation:** Zizhao Lao; Qian Yan; Wengjiang Zheng; Yanni Lai; Peiwen Zhou. **Methodology:** Zizhao Lao; Qian Yan; Wengjiang Zheng. **Project administration:** Zizhao Lao; Geng Li; Xiaohong Liu; Yong Jiang. **Resources:** Zizhao Lao; Geng Li; Xiaohong Liu; Hongfa Zhuang; Huiting Huang. **Software:** Qian Yan; Wengjiang Zheng; Peng Wu; Chengxin Liu. **Supervision:** Zizhao Lao; Shaofeng Zhan; Li Geng; Xiaohong Liu. **Validation:** Zizhao Lao; Qian Yan; Wengjiang Zheng. **Visualization:** Zizhao Lao; Qian Yan; Wengjiang Zheng. **Writing – original draft:** Qian Yan; Wengjiang Zheng; Yong Jiang. **Writing – review & editing:** Qian Yan; Wengjiang Zheng; Shaofeng Zhan; Li Geng; Xiaohong Liu. All authors have read and agreed to the published version of the manuscript.

ACKNOWLEDGMENTS

We would like to deeply thank and commemorate Professor Wu Jianguo, the former director of the State Key Laboratory of Virology and an outstanding virologist. We have received special training in pathogen management and experiments of dengue and zika virus from teacher Wu's team, and we were instructed by those excellent viral scientists. We will always miss teacher Wu Jianguo. We thank Dr. Jincun Zhao of the First Affiliated Hospital of Guangzhou Medical University, Guangzhou, China, for the gift of mice deficient in the IFN- α/β receptors ($IFNAR^{-/-}C57BL/6$) and Guangdong Provincial Center for Disease Control and Prevention for Asia ZIKV strain (ZIKV KU963796). Thanks for the materials in Graphical Abstract provided by the Figdraw platform. We thank the support of the Lingnan Medical Research Center of Guangzhou University of Chinese Medicine. We thank Professors Xiaohong Liu and Geng Li for her/his kind help in the initiation of this research and her/his selfless assistances. We thank post-doctorate Zizhao Lao, who put forward the viewpoints of this article and provided the Zika virus and the construction method of this animal infection model. We thank the Animal Biosafety Level 2 laboratory (ABSL-2) of the Animal Laboratory Center at Guangzhou University of Chinese Medicine. We thank Guangzhou Genedenovo Biotechnology Co., Ltd for assisting in sequencing and bioinformatics analysis. We thank the reviewers in the field of virology for their multiple detailed reviews of this article. This study was supported by grants from the National Natural Science Foundation of China (Grant No. 82274418), the Key-Area Research and Development Program of Guangdong Province (Grant No. 2020B1111100002), the "Double First-Class" and High-level University Discipline Collaborative Innovation Team Project of Guangzhou University of Chinese Medicine (Grant No. 2021XK16),

the Science, Technology and Innovation Commission of Shenzhen Municipality (Grant No. JSGG20220226090550002), the Technology Research of COVID-19 Treatment and Prevention and Special Project of Traditional Chinese Medicine Application-Research on the platform construction for the prevention and treatment of viral infectious diseases with traditional Chinese medicine (Grant No. 2020KJCX-KTYJ-130), and the Sanming Project of Medicine in Shenzhen (Grant No. SZYSM202106006).

CONFLICTS OF INTEREST

The authors declare no conflicts of interest.

DATA AVAILABILITY STATEMENT

RNA-seq data was deposited on the Gene Expression Omnibus (GEO), <https://www.ncbi.nlm.nih.gov/geo/query/acc.cgi?acc=GSE213898>.

ETHICS STATEMENT

All animal procedures were approved by the Animal Ethics Committee of Guangzhou University of Chinese Medicine (No. 20220110005).

ORCID

- Qian Yan  <http://orcid.org/0000-0002-2892-7145>
- Wenjiang Zheng  <http://orcid.org/0000-0001-5234-0339>
- Yong Jiang  <http://orcid.org/0000-0002-3609-2280>
- Peiwen Zhou  <https://orcid.org/0000-0002-3755-4037>
- Yanni Lai  <http://orcid.org/0000-0002-9715-5871>
- Chengxin Liu  <https://orcid.org/0000-0002-6612-3412>
- Peng Wu  <https://orcid.org/0000-0003-0447-023X>
- Hongfa Zhuang  <https://orcid.org/0000-0002-1369-1969>
- Huiting Huang  <https://orcid.org/0000-0001-5363-0442>
- Geng Li  <https://orcid.org/0000-0002-2441-2427>
- Shaofeng Zhan  <https://orcid.org/0000-0002-7978-1318>
- Zizhao Lao  <https://orcid.org/0000-0002-6022-5530>
- Xiaohong Liu  <http://orcid.org/0000-0003-4795-3039>

REFERENCES

- Petersen LR, Jamieson DJ, Powers AM, Honein MA. Zika virus. *N Engl J Med.* 2016;374(16):1552-1563.
- Cao-Lormeau VM, Roche C, Teissier A, et al. Zika virus, French polynesia, South pacific, 2013. *Emerging Infect Dis.* 2014;20(6):1084-1086.
- Dowall SD, Graham VA, Rayner E, et al. A susceptible mouse model for Zika virus infection. *PLoS Neglected Trop Dis.* 2016;10(5):e0004658.
- Campos GS, Bandeira AC, Sardi SI. Zika virus outbreak, Bahia, Brazil. *Emerging Infect Dis.* 2015;21(10):1885-1886.
- Musso D, Cao-Lormeau VM, Gubler DJ. Zika virus: following the path of dengue and chikungunya? *The Lancet.* 2015;386(9990):243-244.
- Munoz LS, Parra B, Pardo CA, Neuroviruses Emerging in the Americas Study. Neurological implications of Zika virus infection in adults. *J Infect Dis.* 2017;216(suppl_10):S897-S905.
- Mlakar J, Korva M, Tul N, et al. Zika virus associated with microcephaly. *N Engl J Med.* 2016;374(10):951-958.
- Calvet G, Aguiar RS, Melo ASO, et al. Detection and sequencing of Zika virus from amniotic fluid of fetuses with microcephaly in Brazil: a case study. *Lancet Infect Dis.* 2016;16(6):653-660.

9. Schwartzmann PV, Ramalho LNZ, Neder L, et al. Zika virus meningoencephalitis in an immunocompromised patient. *Mayo Clin Proc*. 2017;92(3):460-466.
10. Carteaux G, Maquart M, Bedet A, et al. Zika virus associated with meningoencephalitis. *N Engl J Med*. 2016;374(16):1595-1596.
11. Pielnaa P, Al-Saadawe M, Saro A, et al. Zika virus-spread, epidemiology, genome, transmission cycle, clinical manifestation, associated challenges, vaccine and antiviral drug development. *Virology*. 2020;543:34-42.
12. Danthi P. Viruses and the diversity of cell death. *Annual Review of Virology*. 2016;3(1):533-553.
13. Dixon SJ, Lemberg KM, Lamprecht MR, et al. Ferroptosis: an iron-dependent form of nonapoptotic cell death. *Cell*. 2012;149(5):1060-1072.
14. Xu M, Kashanchi F, Foster A, et al. Hepcidin induces HIV-1 transcription inhibited by ferroportin. *Retrovirology*. 2010;7:104.
15. Fricker M, Qin L, Sánchez-Ovando S, et al. An altered sputum macrophage transcriptome contributes to the neutrophilic asthma endotype. *Allergy*. 2022;77(4):1204-1215.
16. Xia H, Zhang Z, You F. Inhibiting ACSL1-Related ferroptosis restrains murine coronavirus infection. *Viruses*. 2021;13(12):2383.
17. Yan N, Zhang J. Iron metabolism, ferroptosis, and the links with Alzheimer's disease. *Front Neurosci*. 2020;13:1443.
18. Beyrouti R, Adams ME, Benjamin L, et al. Characteristics of ischaemic stroke associated with COVID-19. *Journal of Neurology, Neurosurgery & Psychiatry*. 2020;91(8):889-891.
19. Wang H, Li Z, Niu J, et al. Antiviral effects of ferric ammonium citrate. *Cell Discov*. 2018;4:14.
20. Walter LT, Higa GSV, Ikebara JM, et al. Evaluation of possible consequences of Zika virus infection in the developing nervous system. *Mol Neurobiol*. 2018;55(2):1620-1629.
21. Russo FB, Jungmann P, Beltrão-Braga PCB. Zika infection and the development of neurological defects. *Cell Microbiol*. 2017;19(6):e12744.
22. Lazear HM, Govero J, Smith AM, et al. A mouse model of Zika virus pathogenesis. *Cell Host Microbe*. 2016;19(5):720-730.
23. Chen H, Lao Z, Xu J, et al. Antiviral activity of lycorine against Zika virus in vivo and in vitro. *Virology*. 2020;546:88-97.
24. Chen S, Zhou Y, Chen Y, Gu J. fastp: an ultra-fast all-in-one FASTQ preprocessor. *Bioinformatics*. 2018;34(17):i884-i890.
25. Langmead B, Salzberg SL. Fast gapped-read alignment with Bowtie 2. *Nature Methods*. 2012;9(4):357-359.
26. Kim D, Langmead B, Salzberg SL. HISAT: a fast spliced aligner with low memory requirements. *Nature Methods*. 2015;12(4):357-360.
27. Pertea M, Pertea GM, Antonescu CM, Chang TC, Mendell JT, Salzberg SL. StringTie enables improved reconstruction of a transcriptome from RNA-seq reads. *Nature Biotechnol*. 2015;33(3):290-295.
28. Robinson MD, McCarthy DJ, Smyth GK. edgeR: a bioconductor package for differential expression analysis of digital gene expression data. *Bioinformatics*. 2010;26(1):139-140.
29. Ashburner M, Ball CA, Blake JA, et al. Gene ontology: tool for the unification of biology. *Nature Genet*. 2000;25(1):25-29.
30. Ogata H, Goto S, Sato K, Fujibuchi W, Bono H, Kanehisa M. KEGG: Kyoto Encyclopedia of Genes and Genomes. *Nucleic Acids Res*. 1999;27(1):29-34.
31. Subramanian A, Tamayo P, Mootha VK, et al. Gene set enrichment analysis: a knowledge-based approach for interpreting genome-wide expression profiles. *Proceedings of the National Academy of Sciences*. 2005;102(43):15545-15550.
32. Petitprez F, Levy S, Sun CM, et al. The murine microenvironment cell population counter method to estimate abundance of tissue-infiltrating immune and stromal cell populations in murine samples using gene expression. *Genome Med*. 2020;12(1):86.
33. Wang W, Li G, De Wu Wu, et al. Zika virus infection induces host inflammatory responses by facilitating NLRP3 inflammasome assembly and interleukin-1 β secretion. *Nat Commun*. 2018;9(1):106.
34. Das M, Smith ML, Furihata T, Sarker S, O'Shea R, Helbig KJ. Astrocyte control of Zika infection is independent of interferon type I and type III expression. *Biology*. 2022;11(1):143.
35. da Silva IRF, Frontera JA, Bispo de Filippis AM, Nascimento OJM. Neurologic complications associated with the Zika virus in Brazilian adults. *JAMA Neurology*. 2017;74(10):1190-1198.
36. Figueiredo CP, Barros-Aragão FGQ, Neris RLS, et al. Zika virus replicates in adult human brain tissue and impairs synapses and memory in mice. *Nat Commun*. 2019;10(1):3890.
37. Wu YH, Cui XY, Yang W, et al. Zika virus infection in hypothalamus causes hormone deficiencies and leads to irreversible growth delay and memory impairment in mice. *Cell Rep*. 2018;25(6):1537-1547.e1534.
38. Zucker J, Neu N, Chiriboga CA, et al. Zika virus-associated cognitive impairment in adolescent. 2016. *Emerging Infect Dis*. 2017;23(6):1047-1048.
39. Meier KC, Gardner CL, Khoretonenko MV, Klimstra WB, Ryman KD. A mouse model for studying viscerotropic disease caused by yellow fever virus infection. *PLoS Pathog*. 2009;5(10):e1000614.
40. Pinto AK, Brien JD, Lam CYK, et al. Defining new therapeutics using a more immunocompetent mouse model of antibody-enhanced dengue virus infection. *mBio*. 2015;6(5):e01316-01315.
41. Chen Y, Li Z, Pan P, et al. Cinnamic acid inhibits Zika virus by inhibiting RdRp activity. *Antiviral Res*. 2021;192:105117.
42. Marco-Puche G, Lois S, Benítez J, Trivino JC. RNA-Seq perspectives to improve clinical diagnosis. *Front Genet*. 2019;10:1152.
43. Schneider WM, Chevillotte MD, Rice CM. Interferon-stimulated genes: a complex web of host defenses. *Annu Rev Immunol*. 2014;32:513-545.
44. Wicherka-Pawlowska K, Wrobel T, Rybka J. Toll-like receptors (TLRs), NOD-like receptors (NLRs), and RIG-I-like receptors (RLRs) in innate immunity. TLRs, NLRs, and RLRs ligands as immunotherapeutic agents for hematopoietic diseases. *Int J Mol Sci*. 2021;22(24):13397.
45. Winkler CW, Myers LM, Woods TA, et al. Adaptive immune responses to Zika virus are important for controlling virus infection and preventing infection in brain and testes. *The Journal of Immunology*. 2017;198(9):3526-3535.
46. Jurado KA, Yockey LJ, Wong PW, Lee S, Huttner AJ, Iwasaki A. Antiviral CD8 T cells induce Zika-virus-associated paralysis in mice. *Nat Microbiol*. 2018;3(2):141-147.
47. Mumtaz N, Koedam M, van Leeuwen JPTM, Koopmans MPG, van der Eerden BCJ, Rockx B. Zika virus infects human osteoclasts and blocks differentiation and bone resorption. *Emerg Microbes Infect*. 2022;11(1):1621-1634.
48. Hadian K, Stockwell BR. SnapShot: ferroptosis. *Cell*. 2020;181(5):1188-1188.e1181.
49. Tang D, Kroemer G. Ferroptosis. *Curr Biol*. 2020;30(21):R1292-R1297.
50. Layrolle P, Payoux P, Chavanas S. PPAR gamma and viral infections of the brain. *Int J Mol Sci*. 2021;22(16):8876.
51. Thulasi Raman SN, Latreille E, Gao J, et al. Dysregulation of Ephrin receptor and PPAR signaling pathways in neural progenitor cells infected by Zika virus. *Emerg Microbes Infect*. 2020;9(1):2046-2060.
52. Tang D, Chen X, Kang R, Kroemer G. Ferroptosis: molecular mechanisms and health implications. *Cell Res*. 2021;31(2):107-125.
53. Williams MS, Kwon J. T cell receptor stimulation, reactive oxygen species, and cell signaling. *Free Radic Biol Med*. 2004;37(8):1144-1151.
54. Matsushita M, Freigang S, Schneider C, Conrad M, Bornkamm GW, Kopf M. T cell lipid peroxidation induces ferroptosis and prevents immunity to infection. *J Exp Med*. 2015;212(4):555-568.

55. Elong Ngono A, Vizcarra EA, Tang WW, et al. Mapping and role of the CD8(+) T cell response during primary Zika virus infection in mice. *Cell Host Microbe*. 2017;21(1):35-46.
56. Huang H, Li S, Zhang Y, et al. CD8(+) T cell immune response in immunocompetent mice during Zika virus infection. *J Virol*. 2017;91(22):e00900-17.
57. Dodiya HB, Kuntz T, Shaik SM, et al. Sex-specific effects of microbiome perturbations on cerebral A β amyloidosis and microglia phenotypes. *J Exp Med*. 2019;216(7):1542-1560.
58. Youssef LA, Rebbaa A, Pampou S, et al. Increased erythrophagocytosis induces ferroptosis in red pulp macrophages in a mouse model of transfusion. *Blood*. 2018;131(23):2581-2593.
59. Tao N, Li K, Liu J. Molecular mechanisms of ferroptosis and its role in pulmonary disease. *Oxid Med Cell Longevity*. 2020;2020:1-12.
60. Chang LC, Chiang SK, Chen SE, Yu YL, Chou RH, Chang WC. Heme oxygenase-1 mediates BAY 11-7085 induced ferroptosis. *Cancer Lett*. 2018;416:124-137.
61. Adedoyin O, Boddu R, Traylor A, et al. Heme oxygenase-1 mitigates ferroptosis in renal proximal tubule cells. *American Journal of Physiology-Renal Physiology*. 2018;314(5):F702-F714.
62. Shostak K, Jiang Z, Charloteaux B, et al. The X-linked trichothiodystrophy-causing gene RNF113A links the spliceosome to cell survival upon DNA damage. *Nat Commun*. 2020;11(1):1270.
63. van Swelm RPL, Wetzels JFM, Swinkels DW. The multifaceted role of iron in renal health and disease. *Nature Reviews Nephrology*. 2020;16(2):77-98.
64. Huang B, Wen W, Ye S. Dapagliflozin ameliorates renal tubular ferroptosis in diabetes via SLC40A1 stabilization. *Oxid Med Cell Longevity*. 2022;2022:1-17.
65. Lassègue B, Griendling KK. NADPH oxidases: functions and pathologies in the vasculature. *Arterioscler Thromb Vasc Biol*. 2010;30(4):653-661.

SUPPORTING INFORMATION

Additional supporting information can be found online in the Supporting Information section at the end of this article.

How to cite this article: Yan Q, Zheng W, Jiang Y, et al. Transcriptomic reveals the ferroptosis features of host response in a mouse model of Zika virus infection. *J Med Virol*. 2022;e28386. doi:10.1002/jmv.28386